Wavefront engineering with phase discontinuities: designer interfaces for high performance planar opticalcomponents

Federico Capasso
HARVARD COLLEGE PRESIDENT & FELLOWS OF

08/27/2015
Final Report

REPORT DOCUMENTATION PAGE

The public reporting burden for this collection of information is estimated to average 1 hour per response, including the time for reviewing instructions, searching existing data sources, gathering and maintaining the data needed, and completing and reviewing the collection of information. Send comments regarding this burden estimate or any other aspect of this collection of information, including suggestions for reducing the burden, to the Department of Defense, Executive Service Directorate (0704-0188). Respondents should be aware that notwithstanding any other provision of law, no person shall be subject to any penalty for failing to comply with a collection of information if it does not display a currently valid OMB control number.

PLEASE DO NOT RETURN YOUR FORM TO THE ABOVE ORGANIZATION.

1. REPORT DATE *(DD-MM-YYYY)* 06-30-2015	2. REPORT TYPE Final Performance Report	3. DATES COVERED *(From - To)* 07/01/2012-06/30/2015

4. TITLE AND SUBTITLE
WAVEFRONT ENGINEERING WITH PHASE DISCONTINUATIES: DESIGNER INTERFACES FOR HIGH PERFORMANCE PLANAR OPTICAL COMPONENTS

5a. CONTRACT NUMBER

5b. GRANT NUMBER
FA9550-12-1-0289

5c. PROGRAM ELEMENT NUMBER

6. AUTHOR(S)
Capasso, Federico

5d. PROJECT NUMBER

5e. TASK NUMBER

5f. WORK UNIT NUMBER

7. PERFORMING ORGANIZATION NAME(S) AND ADDRESS(ES)
President and Fellows of Harvard College Office for Sponsored Programs
Richard A. and Susan F. Smith Campus Center, Suite 600
1350 Massachusetts Avenue
Cambridge, MA 02138-3846

8. PERFORMING ORGANIZATION REPORT NUMBER

9. SPONSORING/MONITORING AGENCY NAME(S) AND ADDRESS(ES)
USAF, AFRL DUNS 143574726
AF Office of Scientific Research
875 North Randolph Street, Rm 3112
Arlington, VA 22203

10. SPONSOR/MONITOR'S ACRONYM(S)
AFOSR

11. SPONSOR/MONITOR'S REPORT NUMBER(S)

12. DISTRIBUTION/AVAILABILITY STATEMENT
Approved for public release; distribution is unlimited.

13. SUPPLEMENTARY NOTES

14. ABSTRACT
The PI and his group opened up new directions of research: the generation of vector beams with metasurfaces that control amplitude, phase and polarization of wavefronts, the detection of wavefronts using metasurfaces, new metasurfaces for controlling surface plasmon wavefronts and high performance device applications of metasurfaces on graphene. In the vector beam area they generated radially polarized light with a single nanostructured metasurface and showed broadband operation from the visible to the near infrared. The PI's team designed holographic metasurfaces that detect the orbital angular momentum of vortex beams and integrated them into commercial silicon photodiodes. They studied surface plasmon wakes, showing that they can be steered using a one dimensional metamaterial made of rotated apertures, and demonstrated "fishbone" plasmonic couplers that enable polarization-controlled tunable directional coupling of light into surface plasmon polaritons. Both bidirectional and unidirectional launching of the latter were demonstrated along with polarization-selective coupling in dielectric waveguide with embedded fishbone couplers. They investigated metasurfaces on graphene and observed greatly enhanced performance in detectors and modulators.

15. SUBJECT TERMS
Metasurfaces, Wavefront Detection, Wavefront Control, Optical Vortices, Beam Shaping, Optical Antennas, Plasmonics, Nanophotonics, Metadevices, Polarimetry, Waveguides

16. SECURITY CLASSIFICATION OF:			17. LIMITATION OF ABSTRACT	18. NUMBER OF PAGES	19a. NAME OF RESPONSIBLE PERSON
a. REPORT	b. ABSTRACT	c. THIS PAGE			
U	U	U	UU		19b. TELEPHONE NUMBER *(Include area code)*

Standard Form 298 (Rev. 8/98)
Prescribed by ANSI Std. Z39.18
Adobe Professional 7.0

Reset

INSTRUCTIONS FOR COMPLETING SF 298

1. REPORT DATE. Full publication date, including day, month, if available. Must cite at least the year and be Year 2000 compliant, e.g. 30-06-1998; xx-06-1998; xx-xx-1998.

2. REPORT TYPE. State the type of report, such as final, technical, interim, memorandum, master's thesis, progress, quarterly, research, special, group study, etc.

3. DATES COVERED. Indicate the time during which the work was performed and the report was written, e.g., Jun 1997 - Jun 1998; 1-10 Jun 1996; May - Nov 1998; Nov 1998.

4. TITLE. Enter title and subtitle with volume number and part number, if applicable. On classified documents, enter the title classification in parentheses.

5a. CONTRACT NUMBER. Enter all contract numbers as they appear in the report, e.g. F33615-86-C-5169.

5b. GRANT NUMBER. Enter all grant numbers as they appear in the report, e.g. AFOSR-82-1234.

5c. PROGRAM ELEMENT NUMBER. Enter all program element numbers as they appear in the report, e.g. 61101A.

5d. PROJECT NUMBER. Enter all project numbers as they appear in the report, e.g. 1F665702D1257; ILIR.

5e. TASK NUMBER. Enter all task numbers as they appear in the report, e.g. 05; RF0330201; T4112.

5f. WORK UNIT NUMBER. Enter all work unit numbers as they appear in the report, e.g. 001; AFAPL30480105.

6. AUTHOR(S). Enter name(s) of person(s) responsible for writing the report, performing the research, or credited with the content of the report. The form of entry is the last name, first name, middle initial, and additional qualifiers separated by commas, e.g. Smith, Richard, J, Jr.

7. PERFORMING ORGANIZATION NAME(S) AND ADDRESS(ES). Self-explanatory.

8. PERFORMING ORGANIZATION REPORT NUMBER. Enter all unique alphanumeric report numbers assigned by the performing organization, e.g. BRL-1234; AFWL-TR-85-4017-Vol-21-PT-2.

9. SPONSORING/MONITORING AGENCY NAME(S) AND ADDRESS(ES). Enter the name and address of the organization(s) financially responsible for and monitoring the work.

10. SPONSOR/MONITOR'S ACRONYM(S). Enter, if available, e.g. BRL, ARDEC, NADC.

11. SPONSOR/MONITOR'S REPORT NUMBER(S). Enter report number as assigned by the sponsoring/ monitoring agency, if available, e.g. BRL-TR-829; -215.

12. DISTRIBUTION/AVAILABILITY STATEMENT. Use agency-mandated availability statements to indicate the public availability or distribution limitations of the report. If additional limitations/ restrictions or special markings are indicated, follow agency authorization procedures, e.g. RD/FRD, PROPIN, ITAR, etc. Include copyright information.

13. SUPPLEMENTARY NOTES. Enter information not included elsewhere such as: prepared in cooperation with; translation of; report supersedes; old edition number, etc.

14. ABSTRACT. A brief (approximately 200 words) factual summary of the most significant information.

15. SUBJECT TERMS. Key words or phrases identifying major concepts in the report.

16. SECURITY CLASSIFICATION. Enter security classification in accordance with security classification regulations, e.g. U, C, S, etc. If this form contains classified information, stamp classification level on the top and bottom of this page.

17. LIMITATION OF ABSTRACT. This block must be completed to assign a distribution limitation to the abstract. Enter UU (Unclassified Unlimited) or SAR (Same as Report). An entry in this block is necessary if the abstract is to be limited.

Final Performance Report to AFOSR

AFOSR contract FA9550-12-1-0289
WAVEFRONT ENGINEERING WITH PHASE DISCONTINUITIES: DESIGNER
INTERFACES FOR HIGH PERFORMANCE PLANAR OPTICAL COMPONENTS
Reported period: July 1, 2012- June 30, 2015

PI: Prof. Federico Capasso
President and Fellows of Harvard College
John A. Paulson, School of Engineering and Applied Sciences
Harvard University
205A Pierce Hall
29 Oxford St.
Cambridge MA 02138
Tel. 617-3847611
Fax 617-495-2875
Email: capasso@seas.harvard.edu

1. Objectives

The goal was to carry out research on a new class of optically thin plasmonic metasurfaces based on arrays of optical antennas with spatially varying phase response that will allow unprecedented control of the wavefront of transmitted and reflected light and to explore related device applications across several spectral regions primarily near and mid-infrared.

2. Accomplishments

Metasurface research took off worldwide after publication of the paper by the PI and his group Nanfang Yu et al. "Light propagation with phase discontinuities: Generalized laws of reflection and refraction" *Science* **334**, 333 (2011). In this project, leveraging on this key paper important new directions of research were opened up: the generation of vector beams with metasurfaces that control amplitude, phase and polarization of wavefronts, the detection of wavefronts using metasurfaces, new metasurfaces for controlling surface plasmon wavefronts and finally high performance device applications of graphene.

2a.   Wavefront generation and detection with metasurfaces

Nanostructured Holograms for Broadband Manipulation of Vector Beam

We demonstrated a metasurface which gives simultaneous control over the amplitude, phase and polarization of a light beam over a large spectral range. Our approach combines wavelength scale diffractive holographic apertures with subwavelength structures to create devices that operate broadband. We applied this concept to the generation of radially polarized light with a single nanostructured metasurface by simultaneous manipulation of the phase, amplitude and polarization of the incident beam and showed broadband operation from the visible to the near infrared.

Holographic Detection of the Orbital Angular Momentum of Light with Plasmonic Photodiodes.

We designed holographic metasurfaces that detect specific wavefronts of light such as vortex beams carrying orbital angular momentum. This approach is based on the principle of holography: the coupler is designed as the interference pattern of an incident vortex beam and a focused surface plasmon polaritons (SPP). Upon illumination with the vortex beam a focused SPP

is generated. We integrated these holographic plasmonic interfaces into commercial silicon photodiodes, and demonstrated that such devices can selectively detect the orbital angular momentum of light.

2b.   Metasurfaces for wavefront control of surface plasmon polaritons

Polarization-controlled tunable directional coupling of surface plasmon polaritons

We designed and demonstrated "fishbone" plasmonic couplers that enable polarization-controlled tunable directional coupling of light into surface plasmon polaritons (SPP). Both bidirectional and unidirectional launching of SPPs were demonstrated. These couplers circumvent the limits of conventional prism and grating couplers opening the door to many new applications and investigation of new physics.

Polarization-selective coupling to long-range surface plasmon polariton waveguides

We realized the above polarization-selective coupling scheme in a waveguide. Unidirectional coupling was demonstrated with elliptically polarized light with high left- and right-degree of circular polarization, being coupled to waves launched in opposite directions, respectively. To succinctly describe the polarization-sorting properties of the array we developed a simple formalism based on Stokes device vectors.

Controlled steering of Cherenkov surface plasmon wakes with a one-dimensional metamaterial

We showed that by creating a running wave of polarization along a one-dimensional metallic nanostructure consisting of subwavelength spaced rotated apertures that propagates faster than the SPP phase velocity, one can generate SP wakes, a two-dimensional analogue of Cherenkov radiation. The running wave of polarization travels with a speed determined by the angle of incidence and the incident photon spin angular momentum. By changing either one of these properties we demonstrated controlled steering of the Cherenkov surface plasmon wakes.

2c.   Graphene metasurface phase plates and device applications

Broadband tunable phase plates on graphene

We incorporated metal-insulator-metal structures in plasmonic antenna designs, demonstrating an electrically tunable coupled antenna array on graphene with a record large mid-infrared (MIR) wavelength tuning range (1100 nm, i.e. ~ 20% of the resonance frequency).

Antenna-assisted high responsivity plasmonic-graphene detectors

We demonstrated metallic n a n o antenna structures designed to simultaneously improve both light absorption and photo-carrier collection in graphene detectors. We also elucidated the mechanism of photoconductive gain in these detectors and demonstrated mid-infrared antenna-assisted graphene detectors at room temperature with more than 200 times enhancement of responsivity (~0.4 V/W at λ_0 = 4.45 μm) compared to devices without antennas (<2 mV/W).

*High on-off ratio, high-speed modulators based on tunable metasurface perfect absorber*

We showed that a widely tunable metasurface composed of optical antennas on graphene can be incorporated into a subwavelength-thick optical cavity to create an electrically-tunable perfect absorber. By switching the absorber in and out of the critical coupling condition via the gate bias a modulation depth close to 100% was achieved. We demonstrated ultra-thin (thickness $< \lambda_0/10$) high speed (up to 20 GHz) optical modulators over a broad wavelength range (5-7 µm). The wavelength is scalable from the near-IR to the THz by tailoring the metasurface and the cavity.

3. Wavefront Engineering with Metasurfaces

Optical elements such as lenses, polarizers, attenuators, including diffractive ones, control generally independently amplitude, phase and state of polarization of light so that multiple cascaded optical elements are needed for vector beam manipulation. The ultimate challenge for manipulating a light beam is therefore the control with a single optical element of the vector field, i.e. of the spatial distribution of *amplitude*, *phase* and *state of polarization.* We proposed a new framework for designing metasurfaces that enable simultaneous control of amplitude, phase and polarization. As an example of this approach, we experimentally demonstrated the conversion of circularly to radially polarized light with a single metasurface. This result is noteworthy because it greatly expands the application potential of metasurfaces. For a recent review see P. Genevet and F. Capasso, *Rep. Prog. Phys.* **78**, 24401 (2015).

3a. Nanostructured Holograms for Broadband Manipulation of Vector Beam

Light with an inhomogeneous polarization state, i.e. a spatially varying polarization distribution in the transverse beam cross-section, represents a more general scenario (vector beams) that has started to open up new research opportunities in optics.
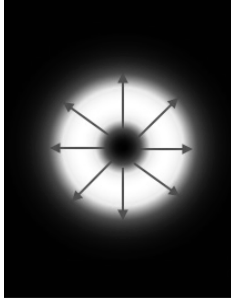

Significant efforts have been devoted to the creation of cylindrical vector beams (CVBs), a family of solutions of the vector wave equation, featuring a cylindrical state of polarization in the dimension transverse to the propagation direction [P. Genevet and F. Capasso, Rep. Prog. Phys. 78, 24401 (2015)]. The radially polarized beam (RPB) is the most widely used free-space CVB (Fig. 1). Due to radial symmetry RPBs have potential for applications in imaging, optical trapping, and laser machining.

Fig. 1 The hollow intensity distribution of a typical radially polarized beam. The arrows indicate the polarization

A radial polarizer, which consists of subwavelength circular metallic gratings as shown in Fig. 2 (a) when illuminated with circularly polarized light yields a far-field intensity pattern that deviates from the desired doughnut shaped RPB (Fig. 2 (a). The additional phase imparted to a light beam in the process of polarization conversion from a circularly-polarized beam to a radially-polarized one using a radial polarizer has a spiral distribution $e^{j\theta}$. The origin of this spiral phase is the projection of the incident light CP light $\overrightarrow{E_{cp}} = \overrightarrow{e_x} + j\overrightarrow{e_y} = e^{j\theta}\left(\overrightarrow{e_r} + j\overrightarrow{e_\theta}\right)$ onto the state of polarization of the light passing through a circular wire-grid polarizer, i.e. the radial state of polarization, such that the output beam profile can be described by $\overrightarrow{E_{out}} = e^{j\theta}\overrightarrow{e_r}$. In order to cancel out the phase factor in the latter expression one can pass the light through a suitable fork hologram which is known to produce vortices with phases $e^{j\theta}$ and $e^{-j\theta}$ in the first order diffraction orders (+1 and -1), Fig. (2b). Thus after grid polarizer and the fork hologram the beams in these two orders are described by $\overrightarrow{E_{out}} = e^{j\theta}\overrightarrow{e_r}\ e^{j\theta}$ and

$\overrightarrow{E_{out}} = e^{j\theta}\overrightarrow{e_r}\ e^{-j\theta}$. The latter is a radially polarized beam with the characteristic donut shape (Fig. 1a). The two patterns can be integrated in a single nanostructured metasurface (Fig 2 (c). , which we designed and fabricated [J. Lin et al. *Nano Lett.* **13,** 4269 (2013)]
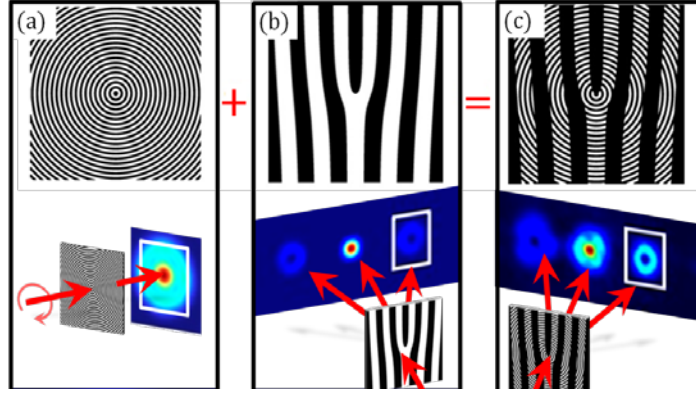
Fig. 2. The technique used to generate radially polarized beams (RPBs) combines sub-wavelength apertures for polarization control and wavelength-scale diffracting apertures. The structure that generates RPBs (c) is the superposition of a radial polarizer (a) and a fork diffraction hologram (b) to cancel the $e^{j\theta}$ phase contribution that arises from the projection of the circularly polarized optical field onto the state of radial polarization, as explained in the text. The black and white colors in the upper row represent respectively "0" (opaque) and "1" (transparent) in the transmittance function of the device. The periods in (a) and (b) are 200nm and 1.2μm, respectively. Shown are also the computed far field intensity distribution using standard Finite Difference Time Domain simulations

Figure 3 summarizes the experimental findings which demonstrate the generation of the radially polarized vortex and that the effect is broadband (visible to near-ir) due to the non-resonant nature of the metallic structures.
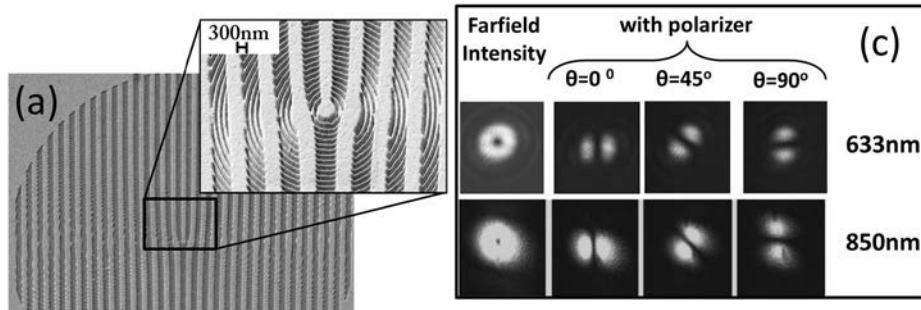

Fig. 3. The fabricated structure (a) was tested with two different wavelengths (633 nm and 850 nm) from a circularly polarized laser beam. The far-field intensity distribution of the +1 diffraction order, captured by a CCD camera after passing through a linear analyzer oriented at varying angles, demonstrates that the vortex is radially polarized

3b. Holographic Detection of the Orbital Angular Momentum of Light with Plasmonic Photodiodes.

Light with orbital angular momentum, also called vortex beams, have a doughnut-like transverse intensity profile and carry an OAM of $\hbar L_i$ per photon, where L_i is the number of twists of the wavefront along a distance equal to the wavelength and $\hbar$ is Planck's constant. L_i is also known as the topological charge of the vortex. OAM beams are appealing for applications in microscopy, optical trapping and optical communication. All methods to detect OAM were free-space based, requiring bulky systems comprising multiple components which are usually not cost effective and are difficult to implement [P. Genevet and F. Capasso, *Rep. Prog. Phys.* **78**, 24401 (2015)].

By using the unique properties of SPPs, we measured the OAM with conventional photodetectors by integrating plasmonic couplers into commercial silicon photodiodes [P. Genevet et al. *Nature Comm.* **3,** 1278 (2012)]. We first computer generated holograms by interfering a converging SPP wave with incoming free-space beams carrying OAM, also known as optical vortex beams (Fig. 4). The resulting pattern was subsequently digitized and transferred on a metallic thin film deposited on the window of a commercial Silicon photodiode. The hologram consists of a distribution of scatterers disposed directly onto the metal surface in the locations where constructive interference between the two waves occurs, that is where the phase of both the incident wave and the SPP are equal (Fig. 4, Left). By illuminating the hologram with the same beam used to generate the pattern, a converging SPP is created. In the focal region of this holographic lens the metal was perforated with a line of subwavelength holes (Fig. 4 Right). The SPP tunnel through the latter following the well-established phenomenon of extraordinary transmission and emerge on the other side of the film as light which is detected by the photodiode (Fig. 4 Right). The resulting detector is high selective since it is designed to detect only vortex beams of a particular OAM.
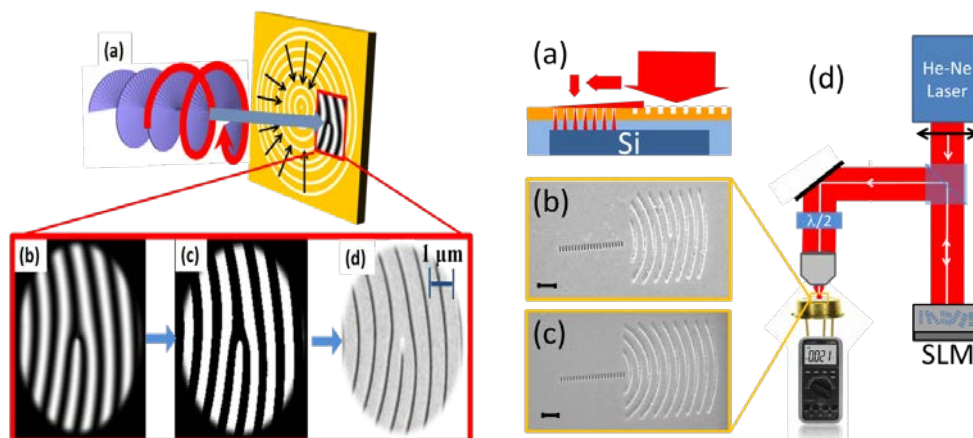
Fig. 4 Left: Interferometric design of the plasmonic couplers (a) Schematic explaining the approach used to design our holographic interfaces. Holographics couplers are designed by considering the interference between the incident beams with a complex wavefront, such as a vortex beam, impinging on the metal interface at normal incidence and converging surface plasmon polariton (SPP) beams. (b) Computer generated interferogram. The incident vortex beam is assumed to be a Gaussian-vortex beam with an optical angular momentum equal to $L_i = -1$. (c) Binary version of the interferogram in (b). The bright lines represent the locations of equal phase of the two beams, where maximum constructive interference occurs. (d) Scanning electron micrograph of a fabricated holographic interface where the grooves are placed at the equi-phase locations. **Right:** Experiment to detect the orbital momentum of a vortex beam with a patterned photodiode. (a) Cross section of the photodiode. The holographic interface couples incident radiation into focused surface plasmons, which are then funneled as light into the detector by an array of sub-wavelength holes. The function of the spatial lightwave modulator (SLM) is to impart to the incident laser beam a spiral-shaped wavefront of well-defined orbital angular momentum. A half-waveplate is used to control the incident polarization. The generated photocurrent is measured with an ammeter.

Fig. 5 (a) shows the response of a photodiode patterned with a hologram created by the interference between a converging SPP and a Gaussian beam. This is a conventional plasmonic lens and is our reference sample. Fig 5(b) presents the same measurements as in (a) but obtained using a photodiode patterned with the hologram designed by interference of converging SPP and an incident vortex beam of charge $L_i = -1$. In (a) the maximum photocurrent is observed for an incident Gaussian beam, i.e. when the incident beam matches the design of the hologram, and the signal decreases considerably (below 10%) for beams with OAM. Conversely, Fig 5(b) shows that the maximum photocurrent is measured for an incident vortex beam with $L_i = -1$.
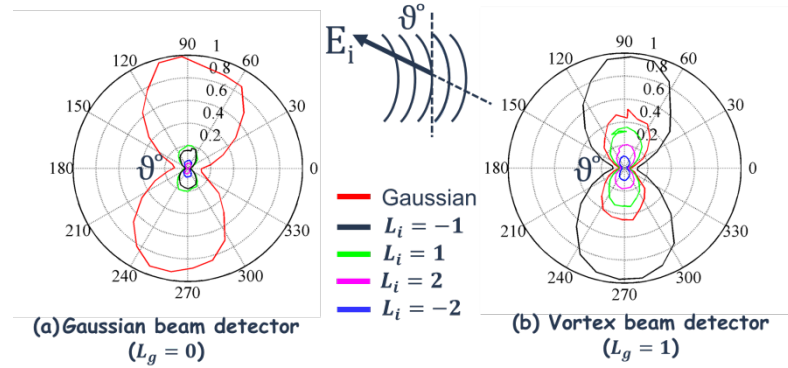

Figure 5 Detected photocurrent as a function of the incident polarization and OAMs. The inset shows the orientation of the incident electric field with respect to the grooves. Photocurrent is measured for two different holographic photodiodes, one patterned with a classical plasmonic lens (Fig. 5 d, $L_g = 0$) that focuses a Gaussian beam (a) and the other with a plasmonic lens (Fig. 4 b, $L_g = 1$) that focuses a vortex beam with $L_i = -1$ (b). Each color denotes a vortex beam with a different topological charge. The inset shows the orientation of the incident electric field with respect to the grooves. Note that $L_g = 1$is the angular momentum provided by the fork hologram to the incident beam on account of conservation of angular momentum.

4**. Surface plasmon polariton wavefront engineering with metasurfaces**

Subwavelength structured surfaces can be used to shape in novel ways surface plasmon polaritons (SPP) beams. Examples are the diffraction-less beams, such as the cosine-Gauss beams previously demonstrated by us [P. Genevet and F. Capasso, *Rep. Prog. Phys.* **78**, 24401(2015)]. New light couplers based on tunable routing of SPP might find future applications in a range of areas such micro/nano particle manipulation and chem/bio sensing.

4a. Polarization-controlled tunable directional coupling of surface plasmon polaritons

Polarization dependent directional launching of SPP was first reported by us with nanostructured fish-bone metagratings [J. Line et al. *Science* **340,** 331 (2013)]. This directional coupling mechanism opens up new opportunities for developing polarization sensitive directional holograms. When an array of apertures in metallic films are arranged in a column with a spacing that is smaller than the SPP wavelength, the launched SPPs are plane waves that propagate perpendicularly away toward either side of the column and emission is obtained independently from the orientation of the dipoles of the column. Therefore it is possible to create a source of SPP plane waves propagating in a fixed direction that can be designed to selectively respond to a polarization component of the incident light, the latter is determined by the orientation of the apertures of the column. Polarization sensitive holographic plasmon couplers can be designed by considering the interference of the SPP waves created by several columns, each having a specific polarization response and arranged following a holographic design discussed in the second paragraph of this paper. For example one can create a directional one dimensional
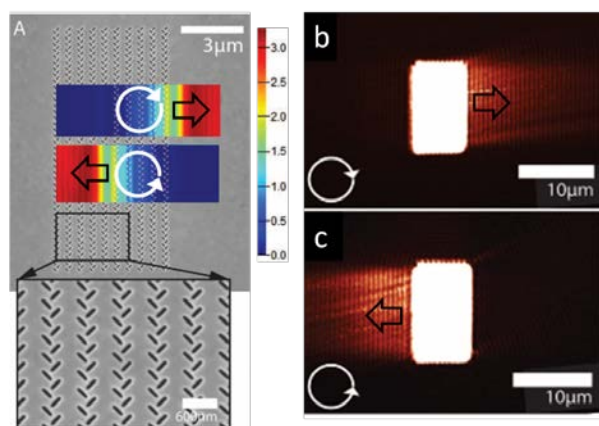
Figure 6. Measurement of the SPPs launched by a fabricated "fishbone" coupler. (A) Scanning electron microscope (SEM) image of a structure fabricated in a gold film for

operation at λ = 633 nm. Overlaid on the SEM image, we present the FDTD simulation of the near-field intensity (arbitrary units) above a coupler made up of five column pairs under illumination by incident light with circular polarizations (white arrows). (b and c) NSOM images of the structure under illumination from the back by right CPL (b), and left CPL (c). The state of incident polarization is shown by white arrows. The fringes arise from interference between the transmitted incident beam through the gold film and the propagating SPPs.

plasmonic coupler by considering a periodic array of two parallel columns, spaced a sub SPP wavelength distance apart and made up of apertures with different orientation. For this specific coupler presented in Fig. 6 the spacing between the two sub units is equal to a quarter of the SPP wavelength and the apertures of the first and second column are oriented at 90 deg. with respect to each other. If light is normally incident on the metal surface, the respective columns will then couple to the two normal components of the incident field. Using circular polarization, the phase retardation between the two normal components transferred to the SPP differs by a phase factor $e^{i\sigma\pm\frac{\pi}{2}}$, where the spin angular momentum $\sigma\pm = \pm1$ whether light is left of right circularly polarized. The propagating phase accumulated by SPP propagating over a distance of a quarter of SPP wavelength is $e^{-i\sigma\pm\frac{\pi}{2}}$ depending on the direction of propagation. Therefore, constructive interference of the SPP waves launched by each column results in time-averaged SPP field intensities propagating to the right or to the left to the pair of columns, depending on the sign of the spin-angular momentum of light.

4b. Polarization-selective coupling to long-range surface plasmon-polariton waveguides

As a model system, we employed long-range SPP (LRSPP) waveguides, which consist of nanometer-thin metal strips embedded in a homogenous dielectric environment [J. Balthasar Mueller et al. *Nano Lett*., **14,** 5524 (2014)]. The guided mode of such waveguides corresponds to the symmetric hybrid mode that arises from the coupling of the SPP modes at the top and bottom surfaces of the metal film as the film thickness is decreased and is always transverse-magnetic (TM) polarized, which eliminates polarization crosstalk within the waveguide. In contrast to conventional SPPs, LRSPPs can achieve centimeter-scale propagation lengths and enable near-perfect mode-matching to optical fibers, as well as simultaneous guiding of electrical and optical signals. Our waveguides were optimized for operation at telecommunication wavelengths and consist of 10 mm wide Au stripes with

a thickness of 15 nm that are embedded in polymer (Fig 7a). The polymer has a refractive index of $n_{BCB} = 1.535$ at 1550 nm. This geometry supports a single TM-polarized mode at C and L band frequencies (λ =1530 nm to 1625 nm) of optical amplifiers used in telecommunications. Waveguides were patterned with UV lithography on top of antenna arrays consisting of subwavelength-spaced rows of 200 nm long, 80 nm wide and 15 nm thick Au rod antennas fabricated with electron-beam lithography. The rows are arranged in pairs with lateral spacing of $\lambda_{LRSPP}/4$, with the antennas oriented at 45 deg with respect to the waveguide axis, giving them their polarization-sorting ability.

The device response is described in terms of the optical power routed to the left and right propagating SPP channels as a function of the incident polarization. The action of any polarization selective device maybe described in terms of projective measurements graphically represented as points on the surface of a sphere (Fig. 7). In optics, this geometric representation is known as the Poincaré sphere.
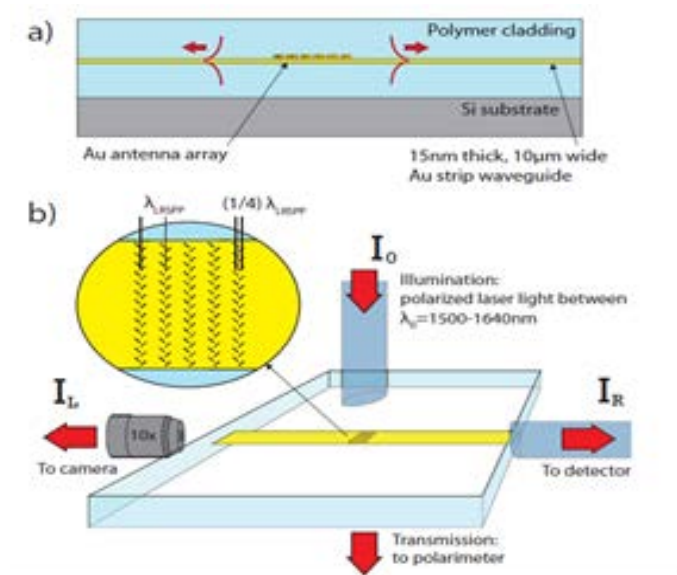
Fig. 7 a) Side view of a gold long-range surface plasmon polaritons (LRSPP) waveguide patterned on top of a polarization-sorting gold antenna array. Under illumination, the antenna array launches LRSPPs propagating to the left and to the right towards the waveguide end facets. b) The polarization response of the devices is measured by observing the light output at the waveguide end-facets as the fishbone coupler is illuminated with light of variable polarization from an optical fiber
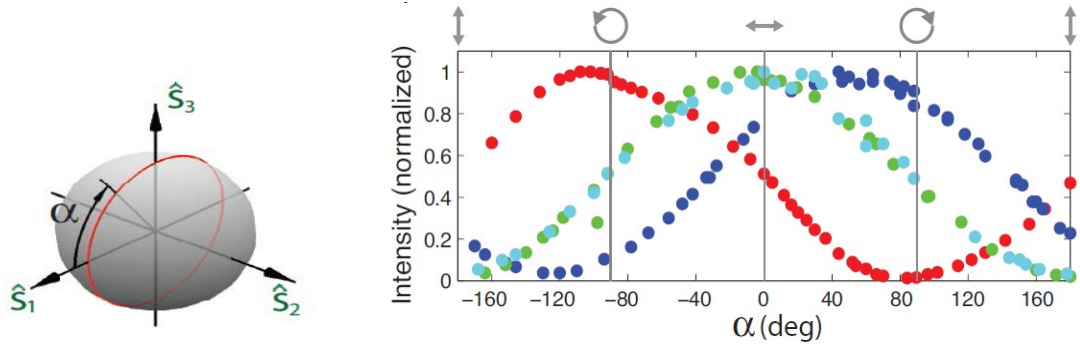
Fig. 8 Left: The states of light are represented by the points on the on the Poincaré Sphere (Stokes vectors). Right circularly polarized light corresponds to the "north pole" and left circularly polarized light to the south pole. **Right** :(dark blue) and right (red) output intensities from the structure as the incident light polarization is varied to trace out a great circle on the Poincaré Sphere in the S1,S3 plane, where the horizontal linear polarization (S1) is taken to be parallel to the waveguide axis. The linear and circular polarization states are marked in grey. Note that the maximum output of the left and right channels is obtained when the incident polarization deviates from the circularly polarized state by ca. 22 deg and 10 deg , respectively. The left- and right outputs of a grating coupler are plotted in green and light blue. The measurements are done at 1550 nm incident wavelength.

Fig 8b (right) displays the normalized left and right outputs of the devices as the input polarization was traced along a great circle around the Poincaré Sphere corresponding to the intersection of the sphere with the S1,S3-plane (Fig 8 Left)). As expected, the output undergoes a sinusoidal variation. However note that unidirectional coupling (maximum output power in one channel and zero on the other) is not obtained for incident states of opposite circular polarization but for the states that somewhat deviate from the latter. We believe that the main contribution to this effect comes from back reflections which introduce phase shifts. We observed unidirectional coupling with extinction ratios of at least 30 dB, limited by the noise. Any other incident polarization state results to a division of the total coupled intensity between the left and right output channel with the total coupled power remaining equal and independent of polarization.

4 c. Controlled steering of Cherenkov surface plasmon wakes with a one-dimensional metamaterial

Whenever a disturbance travels in a medium faster than the phase velocity of the waves it creates, a so-called 'wake' is formed. In fact, this is a general wave phenomenon that accounts for things as diverse as boat wakes, sonic booms, and Cherenkov radiation. In principle, nothing prohibits the existence of SPP wakes; however, creating a disturbance that both excites SPPs and travels faster than their phase velocity is difficult owing to wavevector matching conditions and their light-like nature. In this work we excited a running wave of polarization

(RWP) that travels faster than the phase velocity of the SPPs, and thus are able to create SPP wakes. Furthermore, by employing a metasurface we were able to change the propagation direction of the wakes and steer them in a controllable way.

The RWP is created by having light incident at an oblique angle onto a slit etched in a metal film. Light impinging on different sections of the slit will have different phase because of the different propagation distances (Fig. 9 a,b). This wave, polarized perpendicularly to the slit, excites SPPs and travels with a phase velocity: $c_{RWP}=c/\sin\theta >c_{SPP}$. As can be seen in Fig. 9c, SPP wakes propagate away from the slit at an angle γ given by the equation: $\sin\gamma=\sin\theta/n_{eff}$, In order to controllably steer the wakes, we replace the slit with a series of rotated nanoslits. (Fig.9 d,e).
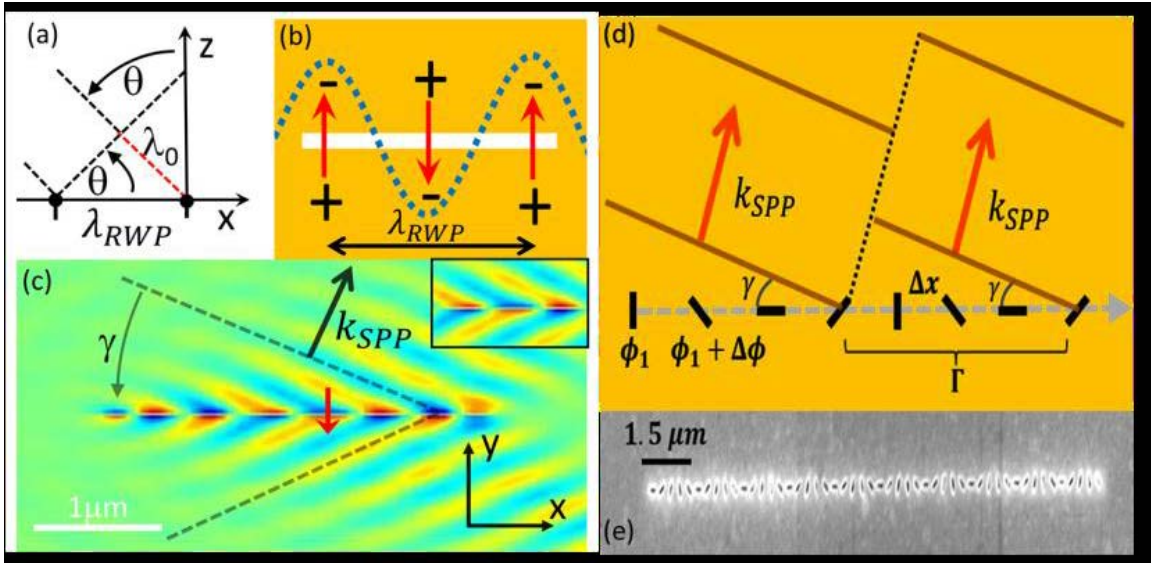
Fig. 9 Running wave of polarization (RWP) and one-dimensional nanostructured metamaterial. (a,b) Light impinging on a slit in a metal film at oblique incidence θ generates a running wave of polarization of wavelength $\lambda_{RWP}= \lambda_0/\sin\theta$ which propagates with a phase velocity: $c_{RWP}=c/\sin\theta>c_{SPP}$, where c is the phase velocity of light in free space and c_{SPP} is the surface plasmon polariton (SPP) phase velocity. (c) Finite difference time domain (FDTD) simulation showing the real part of the electric field E_z 5 nm above the surface. The slit (3 μm long and 50 nm wide) is excited at visible wavelength (610 nm) by a beam incident at $\theta=30°$. It shows the RWP that generates the SPPs, which interfere to form wakes at an angle γ that follows the Cherenkov equation: $\sin\gamma=c_{SPP}/c_{RWP}$. The red arrow denotes the dipole moment at one point along the slit. The inset is a zoomed in view of the slit. (d) Schematic of the creation of SPP wakes by a 1D array of aperture antennas (black rectangles) designed to generate a phase change with constant phase gradient $\Delta\phi\Delta x$ in the emission of SPPs, giving control over the angle of the wakes. The 1D phased array is excited by light incident on the surface at an angle θ, creating the RWP denoted by the grey arrow. Note

that each antenna period, denoted by Γ, creates its own wake (brown lines) which arises from the constructive interference of the wavelets originating from each antenna within the period. The dotted black line corresponds to a line of destructive interference separating the wakes generated by adjacent periods. The angle γ can be controlled by changing $\Delta\phi$, which is proportional to the spatial rotation rate of the antennas $d\alpha(x)dx=\Delta\phi/\Delta x=\pi\Gamma$, where Γ is the period of the elements. (e) Scanning electron micrograph of the nanostructures used to generate the SPP wake.

The rotated apertures allow us to impart a linear phase gradient based on the spatial rotation rate of the apertures when illuminated with circularly polarized light. The dephasing between the x and y components of the polarization causes a dephasing in the excitation of the rotated apertures. This is a geometric phase, commonly called the Pancharatnam-Berry phase.

This results in a modification of the wake equation for the slit giving:

$$\sin\gamma=\sin\theta/n_{eff}\pm(1/k_{SPP})\,\partial\phi\partial x \qquad (1)$$

which can be derived from the schematic in Fig. 9d by imposing the condition that phase shifts between neighboring optical paths (which includes both the incident light path and the SPP path) are equivalent. The $\pm$ is determined by the handedness of the circularly polarized light. In order to verify Eq. 1, we use near-field scanning optical microscopy (NSOM) to probe the near-field of the SPP wakes.

Fig. 10 (left) shows a schematic of the near-field scanning optical microscope (NSOM) setup. A circularly polarized beam is incident at different angles onto the sample. The NSOM signal measured is the interference between the surface plasmons and the transmitted laser light. P, QWP, and TF denote the polarizer, quarter wave plate, and the NSOM tuning fork respectively. T The results are shown in Fig. 10 (right). Side-by-side with the experimental data are the corresponding calculations, where we assume each aperture is a point dipole and employ superposition to sum up the fields of all the dipoles.

This demonstration of SPP wake generation and SPP steering can be further exploited to create new types of plasmonic couplers, such as plasmonic holograms, as demonstrated by us recently [D. Wintz et al. *Nano Lett.* **15**, 3585 (2015)] or directional lenses. Besides connecting this

coupling mechanism with the physics of the Cherenkov effect, our methodology could represent a unique and practical way to test concepts associated with fast travelling perturbations.
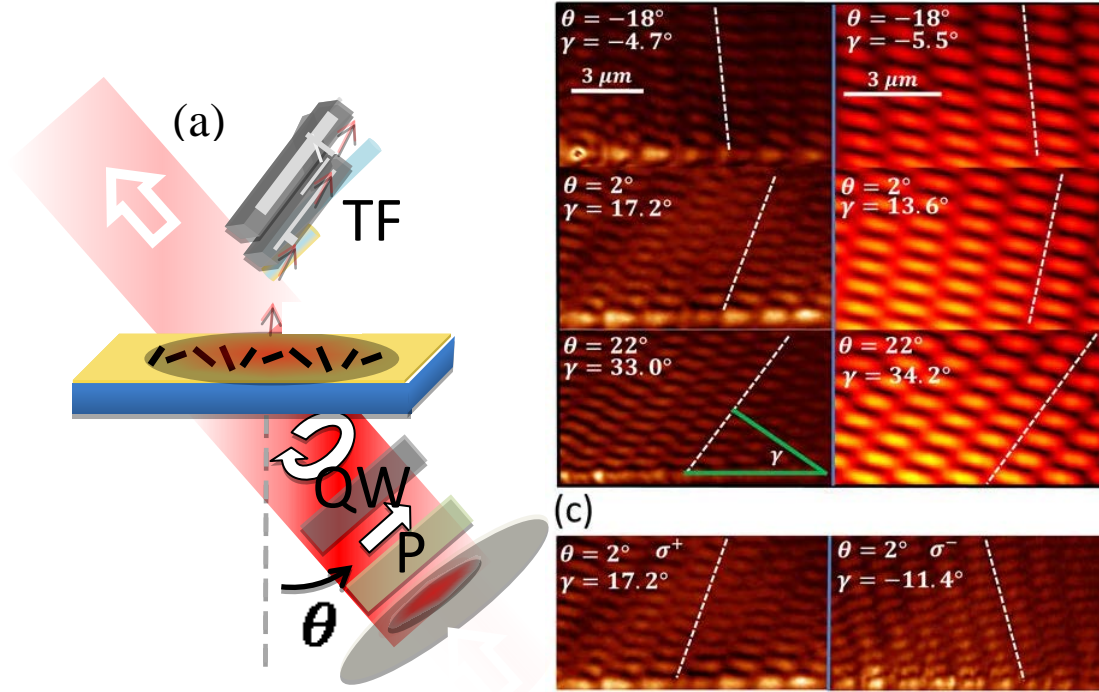
Figure 10 (a) Schematic of the near-field scanning optical microscope (NSOM) setup. (b) Side-by-side comparison between near-field scanning optical microscope images for different angles of incidence and the calculated interference patterns. The linear array of antenna apertures has a period $\Gamma = 1.5\ \mu m$. The dashed lines show the minimum intensity regions parallel to the alleys. The angles γ are obtained from the intersection of the normal to the white dashed lines as shown with the green lines. (c) Comparison between $\sigma+$ and $\sigma-$ polarization showing that for small angles, changing the spin angular momentum of the light reverses the direction of the wakes.

5. **Metasurface phase plates on graphene and device applications**

The use of graphene in metadevices is potentially challenging due to its small thickness and the resultant weak interaction with light. By combining metal and graphene in a hybrid plasmonic structure, it is possible to enhance graphene-light interaction and thus achieve in situ control of the optical response. Highlights of this work have been the demonstration for the first time of a plasmonic-graphene mid-ir high performance device platform which includes: broadband

tunable metasurface phase plates for light beam manipulation, high responsivity detectors and high-speed high on-off ratio modulators.

5 a. Broadband tunable phase plates on graphene.

The reason to use a graphene layer as a tunable materials are several. First, graphene has a wide tuning range, i.e. larger tuning effect. Second, it has a high conductivity which results in high modulation speed, in principle limited by the RC constant of the device. Third, it has very small absorption, around 2%. Finally, it is compatible with Silicon-based fabrication technique and it will easily be stacked up to create multilayered tunable materials. One way to improve the graphene-light interaction is to incorporate graphene in the nano-gap of the end-to-end coupled antennas, where the electric field is greatly enhanced. This end-to-end coupling approach is an effective way to enhance and focus fields into subwavelength volumes. We demonstrated a new type of plasmonic phase plate on graphene comprised of laterally coupled optical antennas, as shown in Fig. 11(a) {Yu Yao et al. *Nano Lett*. **13**, 1257 (2013)}. We found that the plasmonic mode in the coupled-rod region is mainly concentrated in the gap, quite similar to the bonding mode for MIM (metal-insulator-metal) plasmonic waveguide structure. When the charge carrier concentration of graphene underneath the plasmonic structure increases with gate voltage, the graphene permittivity ($\varepsilon = 1 + \frac{i\sigma}{\omega\varepsilon_c}$, where σ is the graphene conductivity) varies, and thus the effective mode refractive index is changed. Compared with the single-stripe waveguide mode, the MIM bonding mode shows an order of magnitude larger change in its effective refractive index, due to the fact that the optical mode is mostly concentrated in the gap, where graphene-light interaction is greatly enhanced, which has been confirmed by the calculation results shown in Fig. 11(b).
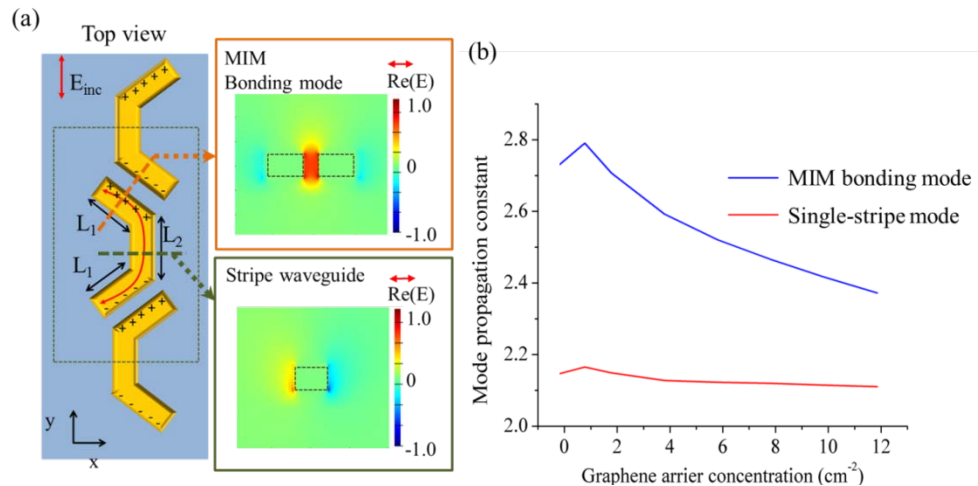
Figure 11. (a) Top view of the laterally coupled plasmonic antennas on a graphene sheet (left) and the electric field distributions of the MIM plasmonic bonding mode (right top) and the single-stripe plasmonic mode (right bottom). L_1 and L_2 are the lengths of the coupling sections and the single-stripe section, respectively. The outline of the waveguide cross-section is given by dashed lines. (b) The effective mode refractive indices (obtained a waveguide solver) of the MIM bonding mode and the single-stripe plasmonic mode (in the antenna resonance wavelength range), respectively. The gap size between coupling sections is 30 nm, the same as that in our experiment. The graphene permittivity is calculated using the random phase approximation (RPA), where the experimentally measured graphene mobility (~2000 cm^{-2}/Vs for our device before doping) is used to obtain the carrier scattering lifetime.

Fig. 12 (a) shows a schematic of the tunable plasmonic phase plate. The device is fabricated on a silicon substrate. A 30 nm silicon oxide layer is grown before graphene transfer. The plasmonic structures and metal contacts were patterned onto the graphene sheet by electron beam lithography (EBL), electron beam evaporation (5 nm Pd and 30 nm Au) and lift-off. Fig.12 (b) shows the scanning electron microscopy (SEM) picture of a portion of the fabricated structure. The reflectance of the samples was measured using a Fourier transform infrared (FTIR) spectrometer with a Mid-IR microscope (NA=0.4). The measured reflectance spectra of one device ($L_1=L_2=480$ nm, coupling gap ~30 nm) are shown in Fig. 12 (c). This record setting wavelength tuning range is ~1100 nm, about 18% of the antenna resonance, which is about twice of that for end-to-end coupled antennas..
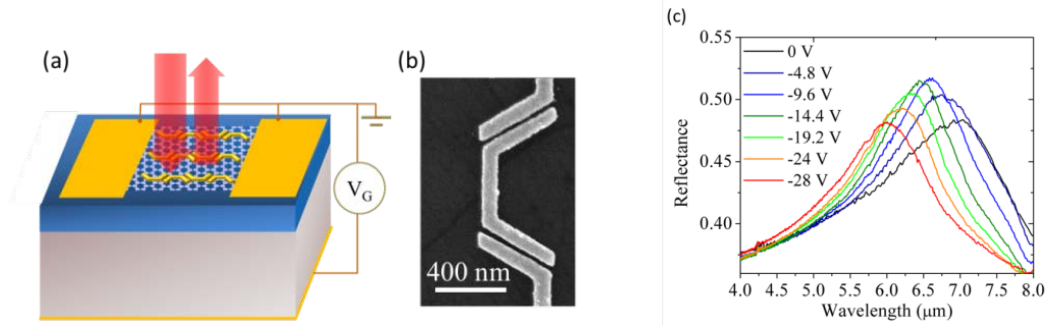
Figure 12 Device configuration and experimental results of the hybrid plasmonic structures (a) schematic of the tunable plasmonic device with a back gate. (b) Scanning electron microscope (SEM) image of the plasmonic structure. (c) Measured reflection spectra from a device after chemical doping of graphene (antenna length $L_1=480$ nm, $L_2=480$ nm, gap size 30 nm, lateral period 2 µm) for different gate voltages (V_G-V_{CNP}). All spectra are normalized to the reflection spectra from a 300 nm Au film evaporated on the same substrate.

## 5 b. Antenna-assisted high responsivity fast plasmonic-graphene detectors

Current mid-IR detectors (PbSe, HgCdTe and quantum well infrared photodetectors (QWIPs)) rely on either semiconductor heterostructures or crystalline films, which are not CMOS compatible. Graphene can absorb photons from the ultraviolet (UV) to the far-infrared (FIR) and can be deposited onto a variety of substrates. Ultrafast graphene photodetectors in the near

infrared (near-IR) have been demonstrated with a bandwidth of over 40 GHz. Therefore, graphene is a promising alternative for mid-IR detectors because of its broadband absorption, high speed, and compatibility to silicon technology. Based on the idea of using coupled optical antennas to enhance photon absorption, due to the high plasmonic field enhancement in the nanogaps of the coupled antennas and photocarrier collection, we demonstrated room temperature mid-infrared (mid-IR) graphene detectors with more than 200 times enhancement of responsivity (0.4 V/W) compared to devices without antennas [Yu Yao et al. *Nano Lett.,* **14,** 3749 (2014)]. In our experiment, we designed free-space graphene detectors with end-to-end coupled antenna structures (antenna length 900 nm, gap size 60 nm) in a 2D array to increase the light collection cross-section, as shown in Fig. 13 (a). The lateral period of the array is chosen to be 1.2 µm so that the constructive interference between scattered light (at antenna resonance wavelength 4.5 µm) from adjacent rows of antennas leads to a high field enhancement and thus maximize the light absorption. The wavelength dependent responsivity of the antenna-assisted graphene detector is measured with a wavelength tunable QC laser (wavelength range: 4.3 µm to 4.7 µm). Due to the resonant nature of the plasmonic antennas, the responsivity (photo-voltage divided by the total incident power on the sample) exhibits strong wavelength dependence, as shown in Fig. 13 (b). The responsivity reaches its maximum around 4.45 µm, which is very close to the peak wavelength (4.46 µm) of the electric field enhancement in the antenna gap calculated with FDTD simulation, also shown in the lower panel of Fig. 12 (b).

The detector responsivity is also dependent on the bias of the detector, because the source drain bias influences the electric field within the graphene channel between adjacent antenna electrodes. Fig.13 (c) shows the responsivity as a function of the bias current (I_{DS}) at room temperature. As the bias current becomes larger, the responsivity increases monotonously and reaches its maximum ($R_V \approx 0.4$ V/W) at $I_{DS} \approx 10$ mA (Further increasing the bias leads to reduced responsivity, probably because the electric field in the graphene channel (>2 MV/m) reaches its breakdown field).

A comparison between the photo-response of the graphene detectors with and without antennas is shown in Fig. 13 (d). With antenna-enhanced photo-carrier generation and collection, the photo-voltage is increased by more than 200 times compared to that of the reference sample at the same laser power. Moreover, the antenna assisted graphene detector shows a linear photo-response as the incident laser power increases to 16 mW, indicating that the absorption is not saturated despite the strong field enhancement in the antenna gaps. Finally we demonstrated experimentally

that the detector response time is fast, limited by the device geometry to ~ 60 ns decay and rise times. Simulations show that owing to intrinsic high sped response of graphene orders of magnitude faster detector speed will be possible with suitable device design.
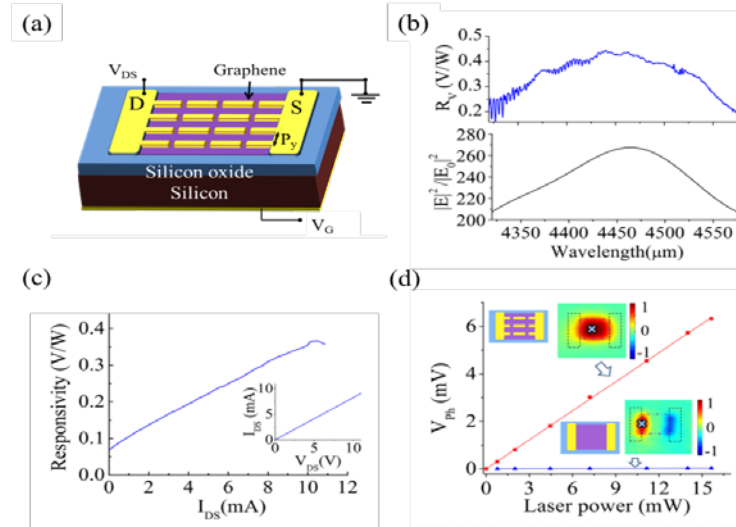

Figure 13 Device characterization of the antenna-assisted graphene detector. (a) A 3D schematic of the antenna-assisted graphene photodetector on a silicon substrate. (b) Measured wavelength dependent photo-response of the antenna-assisted graphene detector (top) and electric field intensity enhancement in the center of the nano-gap between the plasmonic antennas obtained with FDTD simulation (bottom). The narrow dips on the photo-response curve are due to absorption lines of gas molecules in the air or on the sample (mainly CO_2). (c) Measured responsivity of the antenna-assisted graphene detector as a function of the biased current I_{DS} at V_{GS}=4 V. The inset shows the V_{DS}-I_{DS} plot of the same detector when the laser is off. (d) Measured photoresponse of the graphene detectors with and without antennas as a function of incident laser power. The crosses show the positions of the light spot on the sample during the measurement.

5c. High on-off ratio, high-speed modulators based on tunable metasurface perfect absorber

In the broadband tunable metasurface plasmonic phase plate on graphene (Fig. 12 (a)) the modulation depth is limited mainly because the reflection from silicon surface leads to a large reflection background. To achieve high modulation depth, we incorporated the tunable metasurface consisting of the plasmonic array on graphene into a tunable perfect absorber configuration by properly adjusting the dielectric thickness [Yu Yao et al. *Nano Lett.*1**4**, 6526 (2014)]. Fig.14 (a) shows the cross section view of the structure. It is composed of a metallic back reflector, a spacer layer made of dielectric insulators and the tunable metasurface very similar to the one of Fig. 13(a). When the output coupling loss is equal to the cavity internal loss

at the resonant wavelength λ_R, the critical coupling condition is satisfied and the reflection at λ_R from the structure diminishes, which corresponds to the "off" state in Fig. 14 (b). Meanwhile, the metallic reflector also acts as the back gate and spacer layer as the gate dielectric for the tunable metasurface. The antenna resonance wavelength is tuned away from the critical coupling condition by changing the gate voltage, so that the reflection at λ_R increases. Fig. 14 (b) also shows the reflectance from the same structure at a gate voltage V_G-V_{CNP}=-28 V, where V_{CNP} is the charge neutrality point of the graphene sheet. One can see that the reflectance at λ_R increases to more than 60%, more than 30 times of that at V_G-V_{CNP}=0 V. The estimated modulation depth $\Delta R/R_{ON}$ is about 97%.
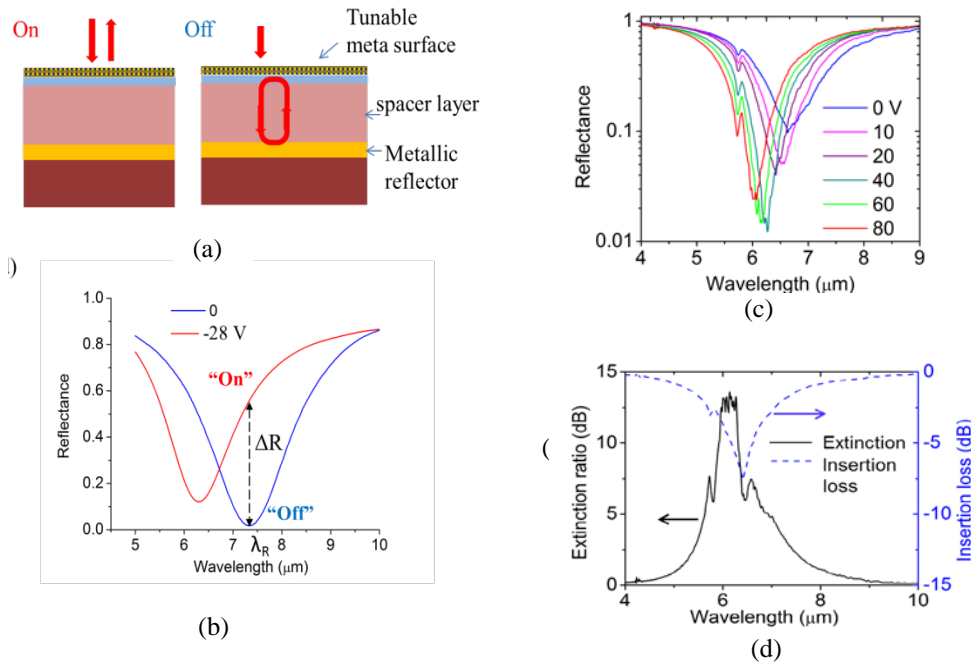
Figure 14 Design of the mid-IR modulator based on tunable perfect absorber. (a): The cross-section view of the tunable perfect absorber based on tunable metasurface, red lines arrows represent light path. The spacer layer is made of dielectric insulator, e.g., aluminum oxide. This layer is inserted in the design and fabrication between the Silicon Dioxide layer, underneath the graphene, and the back metal contact of the phase plate of Fig. 1 (a), forming a lossy cavity that acts as perfect absorber ("off state") at the right bias (- 28 V). (b) Calculated reflectance of the tunable perfect absorber at different gate voltages. (c) Measured reflectance spectra from a device as in (a) for different V_G-V_{CNP}. The voltage of minimum reflectance is different from the one in the simulations due to different device parameters. (d) Measured extinction ratio of the mid-IR modulator.

The whole structure was fabricated on silicon substrate. 300 nm Aluminum was first evaporated onto the surface of the silicon wafer, followed by atomic layer deposition (ALD) of 300 nm aluminum oxide (AlOx). Then a monolayer graphene sheet (grown via Chemical Vapor Deposition (CVD)) was transferred onto the AlOx layer. The antenna array was fabricated on the

graphene sheet by electron beam lithography (EBL), electron beam evaporation of 10 nm Pd and 30 nm Au, and lift-off.

Fig. 14 (c) shows the measured wavelength dependent reflectance of the mid-IR modulator for different bias voltages, from which we obtained the extinction ratio and insertion loss for the modulator at different wavelength, as shown in Fig. 14 (d). The maximum measured extinction ratio (>13 dB) was achieved over 300 nm around the wavelength 6 µm. The operating wavelength region can be flexibly designed by adjusting the dimension of the optical antennas over the whole mid-infrared wavelength range. The extinction ratio can be further increased by optimizing the structure and minimizing the reflectance minimum around the critical coupling condition. High speed measurement showed response times in the nanosecond range limited by the device design. Such speed could be improved by at least 2 orders of magnitude with future work.

6. Publications

[1] P. Genevet, D. Wintz, A. Ambrosio, A. She, R. Blanchard and F. Capasso, "Controlled steering of Cherenkov surface plasmon wakes with a one-dimensional metamaterial" *Nature Nanotechnology* doi:10.1038/nnano.2015.137. Published online 06 July 2015

A *News and views* article on this paper was published in the same issue: H. Chen, Z. Duan, & M. Chen "Metamaterials: Steering surface plasmon wakes" *Nature Nanotechnology* doi:10.1038/nnano.2015.138.

[2] Daniel Wintz, Patrice Genevet, Antonio Ambrosio, Alex Woolf, and Federico Capasso "Holographic Metalens for Switchable Focusing of Surface Plasmons" *Nano Lett*. **15**, 3585 (2015)

[3] Bernhard J. Bohn, Martin Schnell, Mikhail A. Kats, Francesco Aieta, Rainer Hillenbrand, and Federico Capasso "Near-Field Imaging of Phased Array Metasurfaces" *Nano Lett.*, **15,** 3851 (2015)

[4] Patrice Genevet and Federico Capasso, "Holographic optical metasurfaces: a review of current progress", *Rep. Prog. Phys.* **78,** 24401 (2015) http://iopscience.iop.org/0034-4885/78/2/024401 *Invited Review*

[5] Yu Yao, Raji Shankar, Mikhail Kats, Yi Song, Jing Kong, Marko Loncar, Federico Capasso "Electrically Tunable Metasurface Perfect Absorbers for Ultrathin Mid-Infrared Optical Modulators" *Nano Lett.*1**4**, 6526 (2014)

[6] J. P. Balthasar Mueller, Kristjan Leosson, and Federico Capasso "Polarization-Selective Coupling to Long-Range Surface Plasmon Polariton Waveguides" *Nano Lett*., **14,** 5524 (2014)

[7] Yu Yao, Raji Shankar, Patrick Rauter, Yi Song, Jing Kong, Marko Loncar, and Federico Capasso "High-Responsivity Mid-Infrared Graphene Detectors with Antenna-Enhanced Photocarrier Generation and Collection", *Nano Lett.,* **14,** 3749 (2014)

[8] Nanfang Yu and Federico Capasso "Flat optics with designer metasurfaces" *Nature Materials* **13**, 139 (2014) *Invited Review*

[9] Yu Yao, Mikhail A. Kats, Patrice Genevet, Nanfang Yu, Yi Song, Jing Kong, and Federico Capasso, "Broad Electrical Tuning of Graphene-Loaded Plasmonic Antennas" *Nano Lett*. **13,** 1257 (2013)

 [10] Jiao Lin, Patrice Genevet, Mikhail A. Kats, Nicholas Antoniou, and Federico Capasso, "Nanostructured Holograms for Broadband Manipulation of Vector Beams" *Nano Lett.* **13**, 4269 (2013)

[11] J. P. Balthasar Mueller and Federico Capasso "Asymmetric surface plasmon polariton emission by a dipole emitter near a metal surface" *Physical Review* **B 88,** 121410 (2013)

[12] Jiao Lin, J. P. Balthasar Mueller, Qian Wang, Guanghui Yuan, Nicholas Antoniou, Xiao-Cong Yuan, Federico Capasso, "Polarization-Controlled Tunable Directional Coupling of Surface Plasmon Polaritons" *Science* **340,** 331 (2013)

[13} Patrice Genevet, Jean Dellinger, Romain Blanchard, Alan She, Marlene Petit, Benoit Cluzel, Mikhail A. Kats, Frederique de Fornel, and Federico Capasso, "Generation of two-dimensional plasmonic bottle beams" *Optics Express* **21**, 10295 (2013)

[14] Patrice Genevet, Jiao Lin, Mikhail A. Kats and Federico Capasso "Holographic detection of the orbital angular momentum of light with plasmonic photodiodes" *Nature Comm*. **3,** 1278 (2012)

7. Patent disclosures

(HU5642) 62/090,172 Achromatic metasurface optical components by dispersive phase compensation
Capasso, Federico; Aieta, Francesco; Kats, Mikhail; Genevet, Patrice

(HU5744) 62/132,432 Polarimeter
Capasso, Federico; Mueller, Jan Philipp Balthasar; Leosson, Kristjan

AFOSR Deliverables Submission Survey

Response ID:4977 Data

1.

1. Report Type

Final Report

Primary Contact E-mail
Contact email if there is a problem with the report.

szatsiorsky@seas.harvard.edu

Primary Contact Phone Number
Contact phone number if there is a problem with the report

617-495-3256

Organization / Institution name

President and Fellows of Harvard College

Grant/Contract Title
The full title of the funded effort.

WAVEFRONT ENGINEERING WITH PHASE DISCONTINUITIES: DESIGNER INTERFACES FOR HIGH PERFORMANCE PLANAR OPTICAL COMPONENTS

Grant/Contract Number
AFOSR assigned control number. It must begin with "FA9550" or "F49620" or "FA2386".

FA9550-12-1-0289

Principal Investigator Name
The full name of the principal investigator on the grant or contract.

Professor Federico Capasso

Program Manager
The AFOSR Program Manager currently assigned to the award

Dr. Gernot Pomrenke

Reporting Period Start Date

07/01/2012

Reporting Period End Date

06/30/2015

Abstract

The PI and his group opened up new directions of research: the generation of vector beams with metasurfaces that control amplitude, phase and polarization of wavefronts, the detection of wavefronts using metasurfaces, new metasurfaces for controlling surface plasmon wavefronts and high performance device applications of metasurfaces on graphene. In the vector beam area they generated radially polarized light with a single nanostructured metasurface and showed broadband operation from the visible to the near infrared. The PI's team designed holographic metasurfaces that detect the orbital angular momentum of vortex beams sund integrated them into commercial silicon photodiodes. They studied surface plasmon wakes, showing that they can be steered using a one dimensional metamaterial made of rotated apertures, and demonstrated "fishbone" plasmonic couplers that enable polarization-controlled tunable directional coupling of light into surface plasmon

polaritons. Both bidirectional and unidirectional launching of the latter were demonstrated along with polarization-selective coupling in dielectric waveguide with embedded fishbone couplers. They investigated metasurfaces on graphene and observed greatly enhanced performance in detectors and modulators.

Distribution Statement
This is block 12 on the SF298 form.

Distribution A - Approved for Public Release

Explanation for Distribution Statement
If this is not approved for public release, please provide a short explanation. E.g., contains proprietary information.

SF298 Form
Please attach your SF298 form. A blank SF298 can be found here. Please do not password protect or secure the PDF The maximum file size for an SF298 is 50MB.

AFD-070820-035_June 2015 8.27.15.pdf

Upload the Report Document. File must be a PDF. Please do not password protect or secure the PDF . The maximum file size for the Report Document is 50MB.

Performance_Report_capasso-15-final.pdf

Upload a Report Document, if any. The maximum file size for the Report Document is 50MB.

Archival Publications (published) during reporting period:

[1] P. Genevet, D. Wintz, A. Ambrosio, A. She, R. Blanchard and F. Capasso, "Controlled steering of Cherenkov surface plasmon wakes with a one-dimensional metamaterial" Nature Nanotechnology doi:10.1038/nnano.2015.137. Published online 06 July 2015
A News and views article on this paper was published in the same issue: H. Chen, Z. Duan, & M. Chen "Metamaterials: Steering surface plasmon wakes" Nature Nanotechnology doi:10.1038/nnano.2015.138.
[2] Daniel Wintz, Patrice Genevet, Antonio Ambrosio, Alex Woolf, and Federico Capasso "Holographic Metalens for Switchable Focusing of Surface Plasmons" Nano Lett. 15, 3585 (2015)
[3] Bernhard J. Bohn, Martin Schnell, Mikhail A. Kats, Francesco Aieta, Rainer Hillenbrand, and Federico Capasso "Near-Field Imaging of Phased Array Metasurfaces"
Nano Lett., 15, 3851 (2015)
[4] Patrice Genevet and Federico Capasso, "Holographic optical metasurfaces: a review of current progress", Rep. Prog. Phys. 78, 24401 (2015) http://iopscience.iop.org/0034-4885/78/2/024401 Invited Review
[5] Yu Yao, Raji Shankar, Mikhail Kats, Yi Song, Jing Kong, Marko Loncar, Federico Capasso "Electrically Tunable Metasurface Perfect Absorbers for Ultrathin Mid-Infrared Optical Modulators" Nano Lett.14, 6526 (2014)
[6] J. P. Balthasar Mueller, Kristjan Leosson, and Federico Capasso "Polarization-Selective Coupling to Long-Range Surface Plasmon Polariton Waveguides" Nano Lett., 14, 5524 (2014)
[7] Yu Yao, Raji Shankar, Patrick Rauter, Yi Song, Jing Kong, Marko Loncar, and Federico Capasso "High-Responsivity Mid-Infrared Graphene Detectors with Antenna- Enhanced Photocarrier Generation and Collection", Nano Lett., 14, 3749 (2014)
[8] Nanfang Yu and Federico Capasso "Flat optics with designer metasurfaces" Nature Materials 13, 139 (2014) Invited Review
[9] Yu Yao, Mikhail A. Kats, Patrice Genevet, Nanfang Yu, Yi Song, Jing Kong, and Federico Capasso, "Broad Electrical Tuning of Graphene-Loaded Plasmonic Antennas"
Nano Lett. 13, 1257 (2013)
[10] Jiao Lin, Patrice Genevet, Mikhail A. Kats, Nicholas Antoniou, and Federico Capasso, "Nanostructured Holograms for Broadband Manipulation of Vector Beams" Nano Lett. 13, 4269 (2013)
[11] J. P. Balthasar Mueller and Federico Capasso "Asymmetric surface plasmon polariton emission by a dipole emitter near a metal surface" Physical Review B 88, 121410 (2013)
[12] Jiao Lin, J. P. Balthasar Mueller, Qian Wang, Guanghui Yuan, Nicholas Antoniou, Xiao-Cong Yuan, Federico Capasso, "Polarization-Controlled Tunable Directional Coupling of Surface Plasmon Polaritons" Science 340, 331 (2013)
[13} Patrice Genevet, Jean Dellinger, Romain Blanchard, Alan She, Marlene Petit, Benoit Cluzel, Mikhail A. Kats, Frederique

de Fornel, and Federico Capasso, "Generation of two-dimensional plasmonic bottle beams" Optics Express 21, 10295 (2013) [14] Patrice Genevet, Jiao Lin, Mikhail A. Kats and Federico Capasso "Holographic detection of the orbital angular momentum of light with plasmonic photodiodes" Nature Comm. 3, 1278 (2012)

Changes in research objectives (if any):

None

Change in AFOSR Program Manager, if any:

None

Extensions granted or milestones slipped, if any:

None

AFOSR LRIR Number

LRIR Title

Reporting Period

Laboratory Task Manager

Program Officer

Research Objectives

Technical Summary

Funding Summary by Cost Category (by FY, $K)

	Starting FY	FY+1	FY+2
Salary			
Equipment/Facilities			
Supplies			
Total			

Report Document

Report Document - Text Analysis

Report Document - Text Analysis

Appendix Documents

2. Thank You

E-mail user

Aug 27, 2015 16:12:13 Success: Email Sent to: szatsiorsky@seas.harvard.edu